https://dx.doi.org/10.1016/j.mattod.2022.04.005

Materials Today • Volume X, Number X • January/February 2022 RESEARCH

Self-Assembly enables Simple Structure Organic Photovoltaics via Green-Solvent and Open-Air-Printing: Closing the Lab-to-Fab Gap

Hua Tang [1,2,3], Jie Lv[2], Kuan Liu [1,*], Zhiwei Ren[1], Hrisheekesh Thachoth Chandran[1], Jiaming Huang[1], Ying Zhang[1], Hao Xia[1], Jafar I. Khan[3], Dingqin Hu[2], Cenqi Yan[1], Jiyeon Oh[4], Shanshan Chen[5], Shenglong Chu[6], Patrick WK Fong[1], Haiyan Chen[2], Zhengguo Xiao[6], Changduk Yang[4], Zhipeng Kan[2], Frédéric Laquai[3], Shirong Lu [2,*], & Gang Li [1,*]

[1] Department of Electronic and Information Engineering, The Hong Kong Polytechnic University, Hung Hum, Kowloon, Hong Kong SAR, P. R. China.
[2] Thin-film Solar Technology Research Center, Chongqing Institute of Green and Intelligent Technology, Chinese Academy of Sciences, Chongqing, 400714, P. R. China
[3] KAUST Solar Center, Physical Sciences and Engineering Division (PSE), Materials Science and Engineering Program (MSE), King Abdullah University of Science and Technology (KAUST), Thuwal, 23955-6900, Kingdom of Saudi Arabia.
[4] Department of Energy Engineering, School of Energy and Chemical Engineering, Perovtronics Research Center, Low Dimensional Carbon Materials Center, Ulsan National Institute of Science and Technology (UNIST), Ulsan 44919, Republic of Korea
[5] Key Laboratory of Low-grade Energy Utilization Technologies and Systems, CQU-NUS Renewable Energy Materials & Devices Joint Laboratory, School of Energy & Power Engineering, Chongqing University, Chongqing 400044, P. R. China.
[6] Department of Physics, CAS Key Laboratory of Strongly-Coupled Quantum Matter Physics, Hefei National Laboratory for Physical Sciences at the Microscale, University of Science and Technology of China, Hefei, Anhui 230026, China
Corresponding authors.
E-mail: K, Liu kuan-lk.liu@polyu.edu.hk, G, Li gang.w.li@polyu.edu.hk, S, Lu lushirong@cigit.ac.cn

Abstract

The ultimate goal of organic solar cells (OSCs) is to deliver cheap, stable, efficient, scalable, and eco-friendly solar-to-power products contributing to the global carbon neutral. However, simultaneously balancing these five critical factors of OSCs toward commercialization is extremely challenging. Herein, a green-solvent-processable and open-air-printable self-assembly strategy is demonstrated to synchronously simplify the device architecture, improve the power conversion efficiency (PCE) and enhance the shelf, thermal as well as light illumination stability of OSCs. The cathode interlayer (CIL)-free self-assembled OSCs exhibit the PCE of 15.5%, higher than that of traditional inverted OSCs of 13.0%, which is among the top values for both CIL-free self-assembled OSCs and open-air blade-coated bulk-heterojunction OSCs. The remarkable enhancements are mainly ascribed to the finely self-assembly, subtly controlled donor/acceptor aggregation rate, and delicately manipulated vertical morphology. Besides, this strategy enables 13.2% efficiency on device area of 0.98 cm^2, implying its potential for scalability. These findings demonstrate that this strategy can close the lab-to-fab gap of OSCs toward commercialized cheap, stable, efficient, scalable, and eco-friendly OSCs.

1. Introduction

The ultimate purpose of photovoltaic technology is to deliver cheap, stable, efficient, scalable, and eco-friendly solar-to-power products contributing to the global carbon neutral.[1-4] Organic solar cells (OSCs), in particular, have arisen as a promising candidate for next-generation photovoltaic technology on account of low-temperature solution processable, short energy payback period and facile manufactured into light-weight, flexible, and semi-transparent solar-to-power products.[5-17] To date, great success has been achieved in terms of the power conversion efficiencies (PCEs) of OSCs (over 18%) attributed to the tremendous efforts in photoactive material designs, device engineering, and device physics.[18-23] Unfortunately, excellent PCE is only one of the key factors to realize the commercialization of OSCs. The long-term stability, green-solvent-processibility, scalability, and low cost of OSCs play equally critical roles.[10,24,25] However, the progress toward these factors still far lag behind that in PCE, and the commercialization of OSCs remains very challenging. Thus, addressing the technique to reduce the gap between efficiency, stability, green-processibility, scalability, and the cost is of significance to facilitate the commercialization of OSCs.

Historically, the research community has dedicated a great effort to continually make OSCs efficient, stable, eco-friendly, scalable while keeping costs low. In 2006, we pioneered the employment of inverted device architecture leading to the enhanced PCE and more importantly the stability.[26] Then, the inverted architecture becomes a must-try device structures with proofs from more advanced OSC systems (e.g. PffBT4T-2OD:EH-IDTBR, PBDB-T:ITIC, and PBDB-TF:IT4F) delivering efficient OSCs with good stability in the following years.[27-29] In 2016, towards the green fabrication of OSCs, a hydrocarbon solvent, namely 1,2,4-trimethylbenzene (TMB) was reported to replace the widely used but environmentally hazardous halogenated solvent chlorobenzene (CB) to fabricate the OSCs based on PffBT4T-C_9C_{13}:$PC_{71}BM$, which have eventually obtained a PCE of 11.7% and stands the top PCE record of binary fullerene OSCs.[30] In 2017, multiple hydrocarbon solvents, including TMB, o-xylene, and mesitylene are demonstrated to replace CB to manufacture PffBT4T-2OD:EH-IDTBR-based inverted OSCs achieving enhanced efficiency, stability, and reproducibility.[31] These results have proven the feasibility of green production in the industry with a high qualified rate of products. In 2018, a self-

organization method is demonstrated to simplify the device fabrication process, reduce the cost for production and enhance the stabilities of PBDB-TF:IT4F nonfullerene OSCs.[29] Specifically, the self-organization method means spin-coating the solution containing both cathode interlayer (CIL) and bulk-heterojunction (BHJ) materials[32,33], meanwhile, based on the higher surface energy and stronger interaction with the indium tin oxide (ITO) surface, CIL material can self-assembly to the near ITO side. Thus, the self-organization method can obtain comparable device efficiency (13.3%) compared to the traditional step-by-step method (13.4%). This method simplifies the production process by reducing one CIL fabrication, cuts the cost by saving the solvent for CIL coating, and enhances the stability by self-assembly of CIL materials which is preferred for mass production in the industry. In 2019, the self-organization method is further introduced to the fabrication of OSCs via open-air doctor-blading, nevertheless, using the toxic halogen solvent.[34] In comparison to spin-coating in nitrogen, open-air doctor-blade printing is much more cost-effective and industrial preferred on account of the requirement of a very tiny amount of 'ink' without sacrificing the device efficiency and also applicable in upscaling of device area.[34-39] However, the commercialization of OSCs needs simultaneously considering the efficiency, stability, green-processibility, scalability, and cost. Closing the lab-to-fab gap is imperatively in need of commercialization and requires further investigation.

In our opinion, the design of the new device architecture for single junction OSC towards commercialization should mainly focus on the following: (1) how to fine-tune and stabilize the vertical morphology towards high efficiency device and stable OSCs; (2) innovations on high quality interface materials such as replacing the unstable hole-transport-layer of PEDOT:PSS towards highly efficient and stable OSCs; (3) Simplifying the device structure while maintain high performance and manufacturability for low cost promise. Herein, a green-solvent-processible and open-air-printable self-organization strategy towards commercialization is demonstrated to simplify the manufacture, enhance the PCE and stability as well as reduce the cost. We combine the self-organization method with the doctor-blade printing technique, select hydrocarbon solvent dissoluble Phen-NaDPO (DPO) as CIL material and provide an alternative way to simplify the manufacturing of OSCs towards industrialization. In comparison to the insolubility nature of widely used PFN, PFN-Br, and PDINO in hydrocarbon solvent, DPO can be easily dissolved by

hydrocarbon solvent together with organic photoactive materials for self-assembled OSCs. The hydrocarbon solvent of o-xylene is utilized to blade-coating the PM6:BTP-ec9:DPO blend in open-air obtaining PCE of 15.5% for simplified self-organization device ('BHJ(DPO)' type), 13.0% for sequentially printed DPO and BHJ device ('DPO/BHJ' type) and 5.8% for the no-CIL device ('BHJ' type). The performance enhancement is mainly ascribed to the self-assembled DPO-rich domain near ITO and finely tuned vertical distribution of PM6 and BTP-ec9 induced by the self-assembly of DPO, with enhanced exciton dissociation and charge collection. In addition, the BHJ(DPO) devices obtain 13.2% efficiency on a device area of 0.98 cm^2, implying its promising potential for the scale-up printing. This strategy significantly improves the shelf, light and thermal stabilities of BHJ(DPO) devices, proving the effectiveness of the self-organization method on delivering highly stable OSCs. Thus, this green-solvent-processed and open-air-printed self-organization method enable efficient, stable, green, scalable, and low-cost PM6:BTP-ec9 OSCs, providing an alternative route to close the lab-to-fab gap towards commercialization.

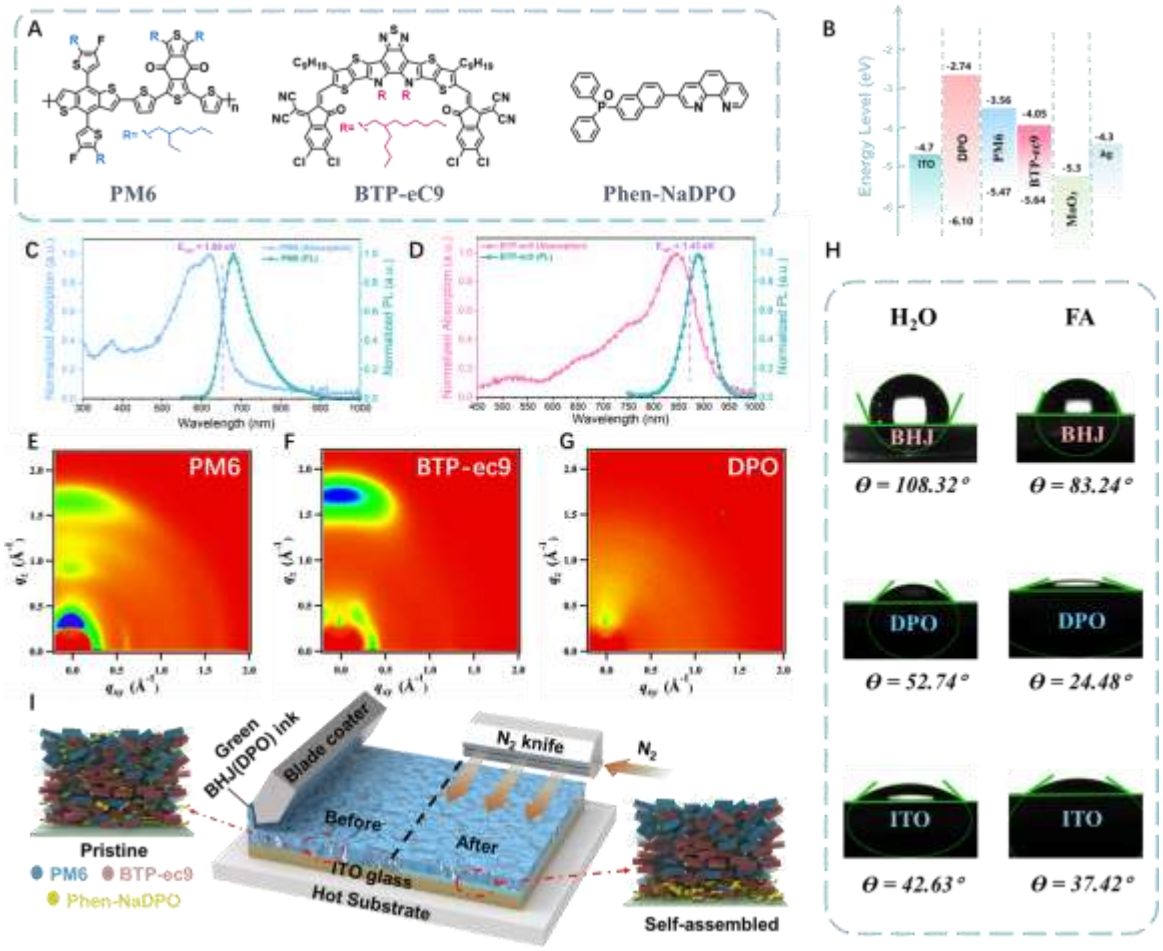

Figure 1. Molecular structures, optical and morphological information of photoactive and CIL materials, and schematic illustration of self-assembled BHJ(DPO) OSCs.

(A) Molecular structures of PM6 and BTP-ec9, and CIL of Phen-NaDPO (DPO). (B) Energy level diagrams of ITO, DPO, PM6, BTP-ec9, MoO_3, and Ag. UV-vis absorption and PL emission spectra of (C) PM6 and (D) BTP-ec9, respectively. 2D Grazing-incidence wide-angle X-ray scattering (GIWAXS) pattern of (E) PM6, (F) BTP-ec9, and (G) DPO. (H). The deionized water and formamide (FA) contact angles of bulk-heterojunction (BHJ) layer, DPO, and ITO. (I) The schematic diagram of green-solvent-processible doctor-blade printed self-organization method.

2. Results and discussion

The optoelectronic properties of PM6, BTP-ec9, and DPO employed in this work are shown in **Figure 1**. The molecular structures of PM6, BTP-ec9, and DPO are presented in **Figure 1A**. **Figure 1B** depicts the energy level diagram of the materials used in the device architecture. DPO possesses the lowest unoccupied molecular orbital (LUMO) level of -2.74 eV and the highest occupied molecular orbital (HOMO) level of -6.10 eV, working as CIL in devices. PM6 possesses the LUMO level of -3.56 eV and the HOMO level of -5.47 eV, which matches well with BTP-ec9 (-4.05 eV/ -5.64 eV).[19,20,40] The optical bandgap (E_{opt}) of PM6 and BTP-ec9 is obtained from the intersection of the normalized UV-vis absorption and PL spectra. As demonstrated in **Figure 1C** and **D**, PM6 and BTP-ec9 possesses the E_{opt} of 1.90 and 1.42 eV, respectively. 2D grazing-incidence wide-angle X-ray scattering (GIWAXS) patterns and their corresponding intensity profiles of PM6, BTP-ec9, and DPO are shown in **Figure 1E-G** and **Figure S3**. The neat film of PM6 exhibits bimodal lamellar peaks in both out-of-plane (OOP) and in-plane (IP) direction at $q_z \approx 0.34$ $Å^{-1}$ and $q_{xy} \approx 0.30$ $Å^{-1}$, and a (010) π-π peak in OOP direction at $q_z \approx 1.67$ $Å^{-1}$, meanwhile, the neat film of BTP-ec9 demonstrates a preferential face-on orientation with a strong (010) π-π peak in OOP direction at $q_z \approx 1.75$ $Å^{-1}$, which are in agreement with the previous reports.[19,20,40] The neat film of DPO presents only a slight response in OOP direction at $q_z \approx 0.33$ $Å^{-1}$ implying its amorphous feature. The contact angles of water and formamide on PM6:BTP-ec9 BHJ blend, DPO, and ITO are tested to obtain their corresponding surface energies. As shown in **Figure 1H** and **Table S4**, the surface energy of the DPO layer (53.08 mJ m^{-2}) is significantly higher than that of PM6:BTP-ec9 BHJ blend (25.43 mJ m^{-2}) but similar to that of ITO (54.77 mJ m^{-2}). Previous works have demonstrated that the large surface energy of CIL materials is the driving force to self-assembly the CIL materials to the ITO surface during the film deposition process of CIL:BHJ blend.[29,34] Considering the large and similar surface energy to ITO, DPO is highly possible to migrate to the near ITO interface during the blade-coating of the DPO:BHJ blend. **Figure 1I** presents the schematic of the green-solvent-processed ambient doctor-blade printing process and the morphology evolvement with the self-assembly of DPO.

The PM6:BTP-ec9 OSCs in this work are doctor-bladed in no-CIL device architecture ('BHJ' type) of ITO/BHJ/MoO_3/Ag, conventional inverted architecture ('DPO/BHJ' type

(means sequential deposition of DPO and BHJ active layer)) of ITO/DPO/BHJ/MoO_3/Ag, and simplified self-assembled CIL-free architecture ('BHJ(DPO)' type (means DPO inside BHJ active layer for self-assembly)) of ITO/BHJ(DPO)/MoO_3/Ag, respectively. **Figure 2A** presents the current density–voltage (*J*–V) characteristics of OSCs printed in these three architectures. The no-CIL device depicts a poor PCE of 5.8% with a low V_{OC} of 0.482V, a J_{SC} of 24.19 mA cm^{-2}, and a fill factor (FF) of 49.9%. The introduction of DPO can significantly enhance the photovoltaic performance of the devices. The PCEs of self-assembled BHJ(DPO) type OSCs (15.5%) with synergistically enhanced V_{OC} of 0.799V, J_{SC} of 26.25 mA cm^{-2}, and FF of 73.6%, outperforming the corresponding DPO/BHJ type OSCs (13.0%) with sequentially coating DPO and BHJ active layers. (**Table 1**) It is worth noting that the self-assembled method effectively alleviates the trade-off between J_{SC} and FF, resulting in the best-performing OSCs among these three architectures. To the best of our knowledge, the green-solvent-processible and open-air-printed self-assembled OSCs we demonstrated are among the best-performing OSCs for both CIL-free self-assembled architecture and open-air doctor-bladed OSCs (**Figure S1, S2**, and **Table S1**).

The external quantum efficiency (EQE) curves of the OSCs printed via different methods are shown in **Figure 2B**. All three devices have presented similar EQE curves, the EQE maximum of the self-assembled BHJ(DPO) type device is 84.1%, higher than the BHJ type of 79.4%, and the DPO/BHJ type of 83.5%. The integrated J_{SC} values of BHJ, DPO/BHJ, and BHJ(DPO) type OSCs are 23.64, 25.14, and 25.51 mA cm^{-2}, respectively, in line well with the J_{SC} values tested from the solar simulator (within a 3% error, **Table 1**). As demonstrated in **Figure 2C (Inset)**, the high-quality large area (9 cm * 10 cm) self-assembled BHJ(DPO) blend film can be obtained via the open-air blade-coating technique, implying the feasibility towards upscaling the self-assembled OSCs. Besides, **Figure 2C (Inset)** also depicts the blade-coated self-assembled BHJ(DPO) devices with an active area of 0.98 cm^2, with negligible deterioration in performance (13.2%), proving the potential of self-assembly strategy for scale-up production.

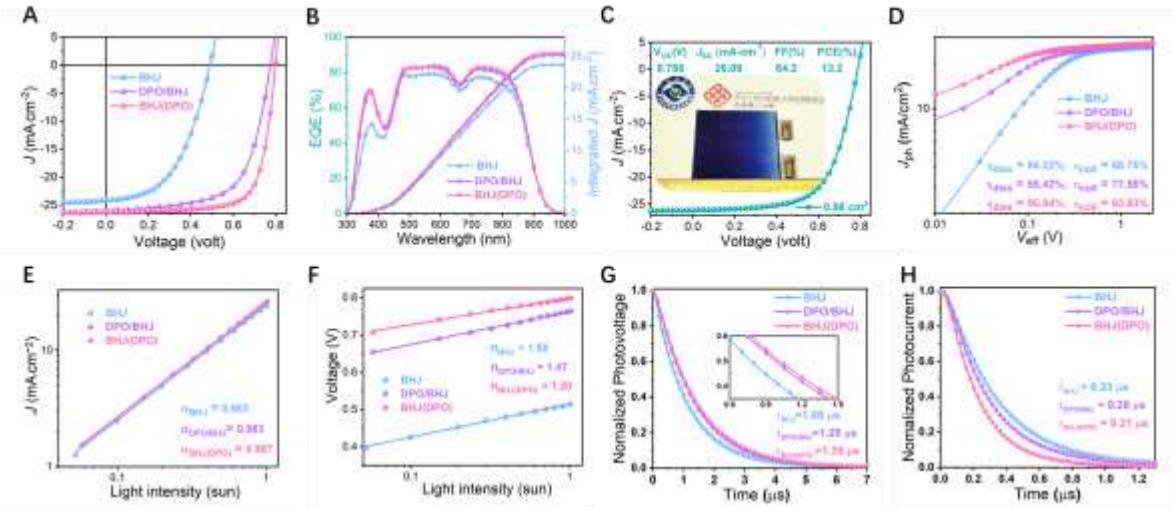

Figure 2. The photovoltaic performance, charge generation, and recombination of OSCs.

(A) *J*–V characteristics of OSCs printed via different approaches. (B) EQE curves of OSCs printed via different approaches. (C) *J*–V curve of self-assembled OSC with an active area of 0.98 cm^2. Inset: digital image of the blade-coated large area (9 cm * 10 cm) self-assembled BHJ (DPO) film and devices (2 cm * 3 cm with an active layer of 0.98 cm^2). (D) Photocurrent density (J_{ph}) as a function of the effective voltage (V_{eff}) of OSCs printed via different methods. (E) J_{SC} versus P_{light} and (F) V_{OC} versus P_{light} of OSCs printed via different approaches. (G) TPV and (H) TPC of OSCs printed via different methods.

Table 1. Summary of photovoltaic performance of green-solvent-processed PM6:BTP-ec9-based OSCs blade-coated in air via various methods under simulated AM1.5G illumination (100 mW cm^{-2}).

Device architecture	V_{OC} [V]	J_{SC} [mA cm^{-2}]	*Calc.* J_{SC} [mA cm^{-2}]	FF [%]	Max PCE [a] [%]
ITO/PM6:BTP-ec9/MoO_3/Ag	0.482	24.19	23.64	49.9	5.8
	0.475 ± 0.016	23.90 ± 0.48		49.3 ± 1.1	5.6 ± 0.2
ITO/DPO/PM6:BTP-ec9/MoO_3/Ag	0.775	26.02	25.14	64.4	13.0
	0.769 ± 0.009	25.92 ± 0.28		63.7 ± 0.8	12.7 ± 0.3
ITO/PM6:BTP-ec9(DPO)/MoO_3/Ag	0.799	26.25	25.51	73.6	15.5
	0.796 ± 0.003	26.19 ± 0.43		72.6 ± 1.4	15.1 ± 0.2

[a] The average values are obtained from 10 devices.

The photocurrent density (J_{ph}) as a function of the effective voltage (V_{eff}) is plotted to unveil the charge generation and extraction mechanism (**Figure 2D**). $J_{ph} = J_L - J_D$, in which J_L is the current density under illumination and J_D is that in the dark. $V_{eff} = V_0 - V_A$, where V_0 is the voltage when J_{ph} is equal to 0, and V_A is the applied bias voltage.[41-47] At a high V_{eff} of 2.5 V, the gross photogenerated excitons are assumed to be dissociated into free charge carriers and then collected by electrodes. The self-assembled BHJ(DPO) device exhibits a saturated current density (J_{sat}) of 27.39 mA cm^{-2}, higher than the DPO/BHJ (27.27 mA cm^{-2}), and BHJ devices (25.60 mA cm^{-2}), which is consistent with the *J-V* curves in these three devices. The exciton dissociation efficiency ($\eta_{diss} = J_{SC}/J_{sat}$) and charge collection efficiency ($\eta_{coll} = J_{max\ power}/J_{sat}$) are calculated under the short-circuit and maximum power output conditions, respectively. The self-assembled BHJ(DPO) device presents a η_{diss} of 95.84% and a η_{coll} of 83.83%, higher than those of the DPO/BHJ (η_{diss} of 95.42% and η_{coll} of 77.56%), and BHJ device (η_{diss} of 94.22% and η_{coll} of 68.75%), indicating self-organization strategy maximizes and balances exciton dissociation and charge collection, in line with the synchronous improvement of J_{SC} and FF in BHJ(DPO) OSCs.

To explore the enhancement of FF using the self-assembled strategy, the charge transport process is investigated. Both hole and electron carrier mobilities are quantified by fitting the space-charge-limited-current (SCLC) model. Hole-only devices are fabricated with the structure of ITO/PEDOT:PSS/active layer/MoO_3/Ag and electron-only

devices with ITO/ZnO/PFN-Br/Active layer/ PFN-Br /Ag. The BHJ(DPO)-based device exhibits the hole mobility of 3.92×10^{-4} cm^2 V^{-1} s^{-1} and electron mobility of 3.67×10^{-4} cm^2 V^{-1} s^{-1}, higher than that of the BHJ-based device (2.22×10^{-4} and 1.97×10^{-4} cm^2 V^{-1} s^{-1}. **Figure S19A-C**), implying the incorporation of DPO plays a positive role on the improvement of the hole and electron mobilities. Besides, the higher and more balanced hole and electron mobilities (μ_e/μ_h = 1.06) leads to the superior FF in the self-organized BHJ(DPO) devices.

To track the destiny of the free charge carriers in the devices, *J*–V characteristics under diverse incident light intensities and the transient photovoltage/photocurrent (TPV/TPC) are tested. Quantitative analysis of the bimolecular recombination losses by employing the power-law relation of $J_{SC} \propto I^{\alpha}$. Specifically, a value of α equal to unity means all the free carriers are swept out and collected at the electrodes before recombination.[46-48] As illustrated in **Figure 2E**, α values of 0.983, 0.983, and 0.987 are obtained for BHJ, DPO/BHJ, and BHJ(DPO) devices, respectively, inferring negligible bimolecular recombination losses for all these systems. On the other hand, the existence of trap-assisted Shockley–Read–Hall (SRH) recombination can be distinguished from the ideality factor *n*. When the V_{OC} was plotted as a function of the incident light intensity, the data follow the expression of $J_{SC} \propto nkT/qln(I)$, where *n*, k is the Boltzmann constant, T is the temperature, and q is the elementary charge, respectively.[45,46,49] Trap-assisted recombination presents if the *n* value deviates from 1 (trap-free condition). The fitted data shown in **Figure 2F** presented *n* values of 1.50, 1.47, and 1.20 for BHJ, DPO/BHJ, and BHJ(DPO) devices, indicating that trap-assisted recombination is efficiently suppressed in the self-assembled BHJ(DPO) device. These results reveal that the self-assembly strategy can notably suppress the density of the trap-assisted recombination center, which contributes to the PCE enhancement of BHJ(DPO) devices.

The charge recombination dynamics and extraction across BHJ active layers could be quantitatively analyzed by TPV and TPC characterizations in devices. The carrier lifetimes (τ) under open-circuit conditions (**Figure 2G**) are extracted from the TPV decay dynamics using mono-exponential fits under a 1 sun bias.[41,42,50] The self-assembled BHJ(DPO) device exhibits a τ value of 1.35 μs, longer than the BHJ and DPO/BHJ counterparts with 1.06 and 1.29 μs, in line with the lowest trap-assisted recombination in the self-assembled

BHJ(DPO) device. The competition between carrier sweep-out and recombination during the operation is obtained through the TPC measurement (**Figure 2H**). The photocurrent decay time under short-circuit conditions is 0.21 μs for the self-assembled BHJ(DPO) device, shorter than that for the BHJ with 0.33 μs and DPO/BHJ device with 0.29 μs, indicating that self-assembly strategy facilitates the charge carrier extraction, in conformity with higher charge collection efficiency of 83.83% in the self-assembled BHJ(DPO) device discussed above (**Figure 2D**).

To unveil the impacts of self-assembly strategy on the morphology manipulation, in-situ UV–vis absorption measurements (**Figure 3A-C**) are carried out to analyze the absorption transition during the solar ink solidification process under the optimal posttreatment condition of thermal annealing at 100℃ for the BHJ, DPO/BHJ and BHJ(DPO) blend films, and the corresponding line-cuts are shown in **Figure S10**. As presented in **Figure 3A-C** and **Figure S10**, it takes 18.9 s for the self-assembled BHJ(DPO) blend film to complete the solidification process, obviously longer than the BHJ of 15.3 s and DPO/BHJ of 12.5 s. Meanwhile, the self-assembled BHJ(DPO) blend film possesses the highest absorption intensity in the whole region, indicating that self-assembly strategy can not only retard the film solidification process but also enhance the film absorption. In addition, the absorption peaks of PM6 and BTP-ec9 in BHJ, DPO/BHJ, and BHJ(DPO) blend films are clearly distinguishable. The peak location and intensity of donor and acceptor are plotted as a function of annealing time to explore donor or acceptor aggregation evolution (**Figure 3E-G**). The PM6 absorption peaks exhibit a red-shift from ~ 606 to 624 nm and the BTP-ec9 absorption peaks also present a red-shift from ~ 732 to 823 nm in all the BHJ, DPO/BHJ, and BHJ(DPO) blend films, consistent with the aggregation process from wet to dry film. The aggregation rate of PM6 and BTP-ec9 can be deduced from the derivative of the peak intensity. Generally, a higher aggregation rate results in irregular orientation and more defects, and a lower aggregation rate leads to oversized domain size and excessive phase separation which are detrimental to the photovoltaic performance.[38,42] As shown in **Figure 3D**, in comparison to the higher aggregation rate of BHJ (0.082 s^{-1} for PM6 and 0.024 s^{-1} for BTP-ec9) and lower rate in DPO/BHJ (0.227 s^{-1} for PM6 and 0.181 s^{-1} for BTP-ec9), the self-assembled BHJ(DPO) blended film presents the moderate aggregation rate of PM6 of 0.101 s^{-1} and BTP-ec9 of

0.122 s^{-1}. In addition, unlike the PM6 exhibits a larger aggregation rate than the BTP-ec9 in BHJ and DPO/BHJ, the self-assembled BHJ(DPO) blend film displays a more balanced rate of PM6 and BTP-ec9. This result indicates the self-assembly of DPO can fine-tune the aggregation rate of both donor and acceptor, contributing to the optimal morphology and enhanced device performance.

GIWAXS is performed to explore the molecular packing and orientation in BHJ, DPO/BHJ, and BHJ(DPO) films, and the corresponding GIWAXS parameters are summarized in **Table S3**. As demonstrated in **Figure 3H-J and Figure S4**, all the three blend films show identical molecular orientations. The self-assembled BHJ(DPO) blend film presents (100) lamellar peaks at q_{xy}≈ 0.25 $Å^{-1}$ with coherence length (CCL) of 3.60 nm and q_z≈ 0.24 $Å^{-1}$ with CCL of 5.28 nm, slightly higher than those of BHJ ((100) lamellar peaks at q_{xy}≈ 0.25 $Å^{-1}$ with CCL of 3.53 nm and q_z≈ 0.24 $Å^{-1}$ with CCL of 5.14 nm) and DPO/BHJ ((100) lamellar peaks at q_{xy}≈ 0.25 $Å^{-1}$ with CCL of 3.55 nm and q_z≈ 0.24 $Å^{-1}$ with CCL of 5.19 nm), indicating that self-assembly strategy can delicately optimize the crystallinity. The (010) π-π stacking of the three blend films shows the identical tendency. (**Figure 3H-J and Figure S4**) The self-assembled BHJ(DPO) blend film displays (010) π-π peaks at q_z ≈ 1.66 $Å^{-1}$ with CCL= 2.78 nm. Meanwhile, the BHJ blend exhibits (010) π-π peaks at q_z ≈ 1.66 $Å^{-1}$ with CCL= 2.53 nm and the DPO/BHJ blend demonstrates (010) π-π peaks at q_z ≈ 1.66 $Å^{-1}$ with CCL= 2.64 nm. The identical molecular orientation and slightly pronounced CCL of both lamellar and π-π peaks in self-assembled BHJ(DPO) blend film validate the effectiveness of self-assembly strategy on delicate morphology control with enhanced crystallinity, leading to the improved hole and electron mobilities, which are beneficial for charge transport.

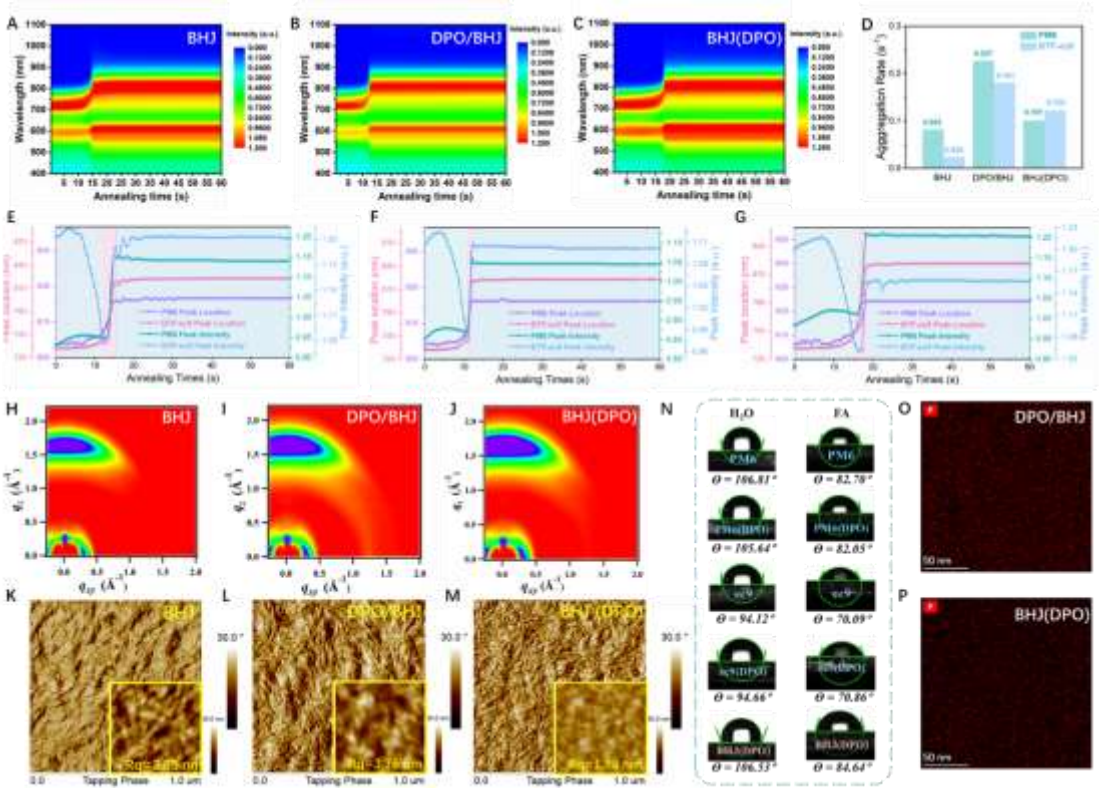

Figure 3. The morphology study of BHJ, DPO/BHJ, and BHJ(DPO) OSCs.

Time-resolved in-situ UV–vis absorption of optimized blend films of (A) BHJ, (B) DPO/BHJ, and (C) BHJ(DPO) under thermal annealing at 100 ℃. (D) The aggregation rate of PM6 and BTP-eC9 in optimized BHJ, DPO/BHJ, and BHJ(DPO) blend films. The peak location and intensity evolution as a function of annealing time of PM6 and BTP-eC9 in (E) BHJ (F) DPO/BHJ, and (G) BHJ(DPO) blend. 2D GIWAXS pattern of (H) BHJ (I) DPO/BHJ, and (J) BHJ(DPO) blend. AFM phase images with height images inset of (K) BHJ (L) DPO/BHJ, and (M) BHJ(DPO) blend. (N) The deionized water and FA contact angles of PM6, PM6(DPO), BTP-ec9, BTP-ec9(DPO), and BHJ(DPO) films. HAADF STEM images of (O) DPO/BHJ, and (P) BHJ(DPO) with EDS mapping of P.

To unveil the effect of self-assembly of DPO on the donor/acceptor phase separation, atomic force microscopy (AFM) is carried out in BHJ, DPO/BHJ, and BHJ(DPO) blend films (**Figure 3K-M**). As displayed in AFM height images, the self-assembled BHJ(DPO) blend film demonstrates a root mean square roughness (R_q) values of 1.88 nm **(Figure 3M (inset))**, lower than that in BHJ (**Figure 3K (inset**), R_q = 3.69 nm) and DPO/BHJ (**Figure 3L (inset**), R_q = 3.79 nm), respectively, which is attributed to the enhanced donor/acceptor miscibility (from 28.27 to 25.19 ($\times 10^{-2}$K (smaller value reflects larger miscibility), **Table S10**) induced by the self-assembly of DPO. As exhibited in **Figure 3N** and **Table S5-6**, the neat films of PM6 and BTP-ec9 show the surface energy of 24.71 and 30.28 mJ m^{-2}, respectively, and the blend films of BHJ (**Figure 1F**, **Table S7**) depict the and 25.43 mJ

m^{-2}, larger than their counterparts containing DPO with PM6(DPO) of 24.52 mJ m^{-2}, BTP-ec9(DPO) of 29.74 mJ m^{-2}, and BHJ(DPO) of 21.93 mJ m^{-2}, implying the incorporation of DPO can effectively decrease the surface energy, which is consistent with the R_q values of AFM height images w/o DPO. Besides, when compared with the phase images in BHJ and DPO/BHJ, the self-assembled BHJ(DPO) demonstrates a clearer and more uniform interpenetrate network contributing to the charge transport. On the other hand, the distribution of DPO within the DPO/BHJ and BHJ(DPO) blend films are explored by high angle annular dark field (HAADF) in scanning-transmission (STEM) mode with X-Ray spectroscopy (EDS) mapping, with the distinct element (P) in DPO. As demonstrated in **Figure 3O – P**, both DPO/BHJ and self-assembled BHJ(DPO) enable uniform distribution of DPO, which is beneficial for homogeneous interpenetration and thereby facilitate the charge transport.

Although the DPO/BHJ and BHJ(DPO) possess the same D/A systems as well as CIL materials, a dramatic enhancement has shown in terms of the PCEs from DPO/BHJ of 13.0% to self-assembled BHJ(DPO) of 15.5%. The reason behind the improved PCE of BHJ(DPO) may be attributed to the finely self-organized DPO-rich region and the subtly manipulated vertical PM6/BTP-ec9 phase separation. Hence the photoluminescence (PL) spectra are carried out to firstly decipher the role of DPO in the photoactive layer. As presented in **Figure S16A** and **B**, the PL intensity of the PM6 and BTP-ec9 pristine films is partially quenched by DPO, indicating that the incorporation of DPO in the photoactive layer can facilitate the exciton dissociation. To double-check the effect of DPO in the photoactive layer, time-resolved photoluminescence (TRPL) is carried out to evaluate the PL quenching efficiency (PLQE). As shown in **Figure S17 A-C**, the neat PM6 and PM6(DPO) are measured with a pulsed photoexcitation at 450 nm. For a closer analysis, the PL transients are tracked at the respective maxima of the emission peak. The incorporation of DPO into the PM6 shortened the PL lifetime moderately from 120 to 112 ps, resulting in PLQE of 7% (calculation equation: $1-\tau_{(PM6(DPO))}/\tau_{(PM6)}$). Herein, we fitted the decay using a bi-exponential decay function and extracted the weighted average lifetimes. In addition, the BTP-ec9 and BTP-ec9(DPO) were tested following a photoexcitation at 710 nm (**Figure S17 D-F**). The incorporation of DPO reduced the PL

lifetime significantly from 180 to 98 ps, leading to a PLQE of 46%. These results are in line with the steady state PL data, indicating the introduction of DPO in the photoactive layer is beneficial for exciton dissociation.

Then, the time-of-flight secondary ion mass spectrometry (TOF-SIMS) is performed to explore the vertical distribution of DPO. The DPO/BHJ and BHJ(DPO) blend films are blade-coated on the ITO surface. Since the ITO contains the distinct element of InO^- and DPO contains the unique component of PO_3^-, the tracking of PO_3^- can reflect the vertical distribution of DPO, meanwhile the emergence of InO^- means the ITO surface is approaching. As shown in **Figure 4A**, the PO_3^- in DPO/BHJ and BHJ(DPO) both emerges very close to the ITO surface, while the intensity of PO_3^- in BHJ(DPO) is obviously higher than that in DPO/BHJ, indicating the DPO in BHJ(DPO) blend film can finely self-assembled on the ITO surface and the corresponding local concentration of DPO on the ITO surface is higher than that of the DPO/BHJ blend film. The vertical PM6/BTP-ec9 phase separation can also be unveiled by the TOF-SIMS via detecting the unique ion of F^- for PM6 and CN^- for the acceptor, respectively. As shown in **Figure S18A**, all the three blend films present similar intensity of F^- in the top (close to the anode). The BHJ blend film shows the highest intensity of F^- with the sputter time increasing, whereas the DPO/BHJ and BHJ(DPO) blend films demonstrate relatively lower intensity of F^-. Finally, BHJ(DPO) exhibits the lowest intensity of F^- in the bottom (near the cathode), implying that the self-assembly of DPO manipulate the vertical morphology, enabling lower concentration of PM6 approaching the ITO surface. On the contrary, BHJ(DPO) blend film displays the lowest intensity of CN^- in the top, then demonstrates an uptrend in CN^- intensity with the sputter time increasing (**Figure S18B**). Consequently, the BHJ(DPO) presents the highest intensity of CN^- at the bottom, indicating that the self-assembly of DPO also facilitates the migration of BTP-ec9 toward bottom. We investigate the donor/acceptor ratio of the active layer vertically from anode to cathode by quantitatively analyzing the F^-/CN^- ratio, thus, unveil the relative phase distribution of PM6 and BTP-ec9 in the vertical direction. As displayed in **Figure S18C**, all the three blend films present a similar donor/acceptor ratio in the upper half active layer, whereas BHJ(DPO) blend film start to exhibit a lower F^-/CN^- ratio in the bottom half, implying the self-assembly of DPO

triggers a reorganization of donor/acceptor distribution with more acceptor on the ITO surface.

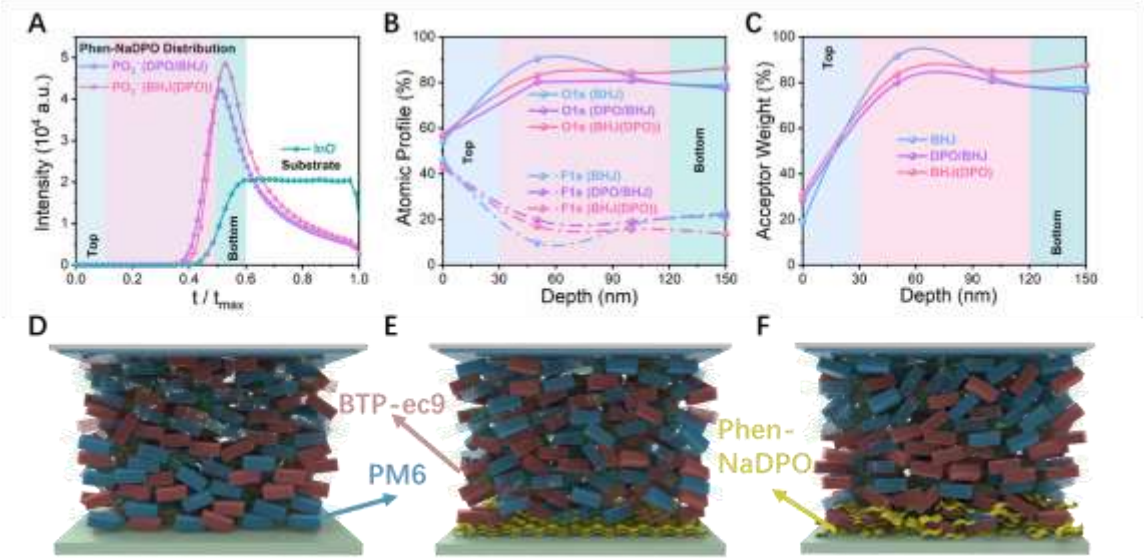

Figure 4. The vertical donor/acceptor phase separation of BHJ, DPO/BHJ, and self-assembled BHJ(DPO) OSCs.

(A) TOF-SIMS ion yield of PO_3^- as a function of sputtering time for DPO/BHJ and BHJ(DPO) blend films. Depth profile XPS of (B) atomic profile of F 1s and O 1s, and (C) acceptor weight as a function of film thickness. The schematic illustrations of the vertical distribution of PM6, BTP-ec9, and DPO in (D) BHJ, (E) DPO/BHJ, and (F) BHJ(DPO) blend films.

To double-check the scenario of vertical phase separation of PM6/BTP-ec9 in the active layers, the depth profile (DP)-X-ray photoelectron spectroscopy (XPS) characterization is carried out to detect the distinct atomic ratio of donor and acceptor. Since the PM6 molecule is composed of a series of D-A repeat units (**Figure 1A**), each repeat unit contains two fluorine (F) and two oxygen (O) atoms, meanwhile, every single BTP-ec9 molecule contains two O atoms. Thus, the acceptor weight content (wt%) at various depths can be calculated by the O/F atom ratio. The atomic profile of O and F are demonstrated in **Figure 4B**, more PM6 are shown at the top while more BTP-ec9 are displayed at the bottom of the BHJ(DPO) blend film, which is in line with the results of TOF-SIMS. As shown in **Figure 4C** and **Table S11**, the acceptor weight in self-assembled BHJ(DPO) blend film exhibits a rising trend, which is perfectly suitable for the self-organized inverted device architecture. On the contrary, in the BHJ and DPO/BHJ blend

films, the acceptor weight shows a parabola-like trend. These results have soundly proven the effectiveness of the self-assembly strategy on the vertical morphology control.

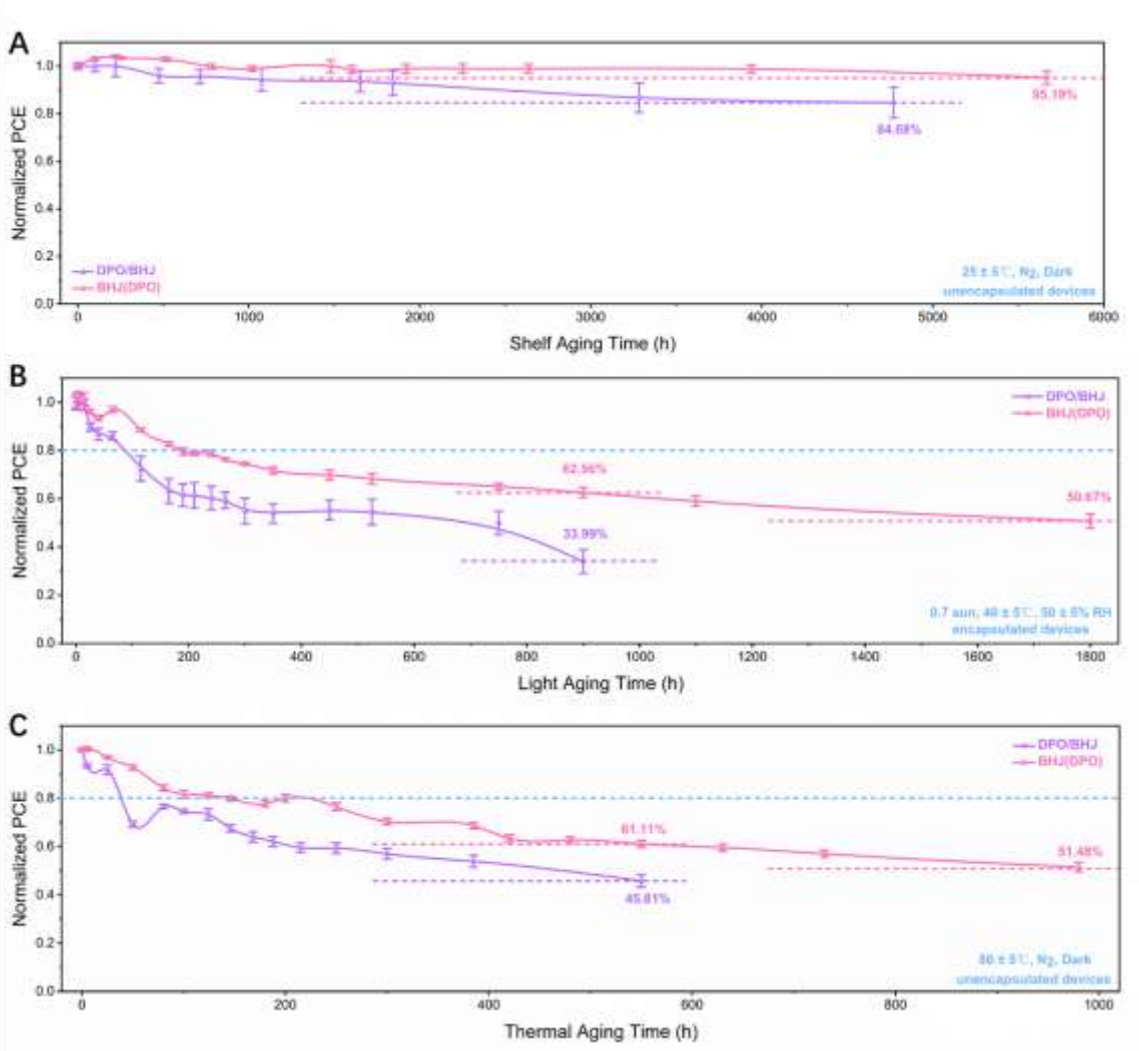

Figure 5. Shelf, light, and thermal stability of OSCs.

(A) Shelf stability of the unencapsulated DPO/BHJ and BHJ(DPO) OSCs shelved in N_2 atmosphere under 25±5℃. (B) Light stability of the encapsulated DPO/BHJ and BHJ(DPO) OSCs exposed under continuous 0.7 sun illumination at 40±5℃ and 50±5% RH. (C) Thermal stability of the unencapsulated DPO/BHJ and BHJ(DPO) OSCs under 80±5℃ in N_2 atmosphere. Data are represented as the mean value and the standard deviation from 5 devices in each condition.

Inspired by the self-assembly of DPO-induced vertical morphology analysis, the schematic illustrations of BHJ, DPO/BHJ, and BHJ(DPO) are proposed in **Figure 4D-F**. The corresponding PM6, BTP-ec9, and DPO distribution are based on the TOF-SIMS and

DP-XPS results. As presented in **Figure 4F**, relatively more PM6 are demonstrated next to the anode side and more BTP-ec9 are shown close to the cathode side compared to BHJ (**Figure 4D**) and DPO/BHJ (**Figure 4E**). Besides, in comparison to the DPO layer in DPO/BHJ, the self-assembled BHJ(DPO) exhibits a thicker DPO-rich 'layer' co-existing harmoniously with PM6 and BTP-ec9 on the ITO surface. These morphology data systematically unveil the nature of self-assembly of DPO-induced vertical morphology manipulation towards high cost-effective and eco-friendly OSCs.

To explore the impacts of self-assembly strategy on the device stability, the storage, light illumination, and thermal stressing of the green-solvent-processed ambient blade-coated DPO/BHJ and self-assembled BHJ(DPO) OSCs are systematically studied under various aging conditions. As shown in **Figure 5A**, the shelf stability is recorded at 25 ± 5°C in the glovebox. The BHJ(DPO) devices exhibit slightly enhanced PCEs in the first ~ 600 h which can be attributed to the continuous self-organization of DPO with vertical morphology optimization. The BHJ(DPO) devices show excellent shelf stability, which still maintains 95.19% of initial PCE after ~ 5700 h, whereas its DPO/BHJ counterpart demonstrates constantly reduced device performance, which only retain 84.68% of initial PCE after ~ 4800 h. The light stability of the encapsulated DPO/BHJ and BHJ(DPO) devices are tracked under continuous illumination (0.7 sun) at 40 ± 5°C and 50± 5% relative humidity (RH). As presented in **Figure 5B**, the T_{80} (80% of initial PCE) lifetime of the self-assembled BHJ(DPO) devices is ~ 190 h, much longer than that of DPO/BHJ devices (~ 90 h). After 900 h light illumination, the BHJ(DPO) devices still maintain 62.56% of the initial device efficiency, much higher than that of DPO/BHJ (33.99%), indicating that the self-assembly strategy is beneficial for reducing the device performance decay under light illumination. In addition, the thermal stability of DPO/BHJ and BHJ(DPO) devices are examined under the 80 ± 5°C in the glovebox. As demonstrated in **Figure 5C**, the self-assembled BHJ(DPO) devices show a T_{80} lifetime of ~ 140 h, much higher than that of DPO/BHJ (~ 36 h), implying the neat DPO layer may be thermally unstable which is detrimental for maintaining the PCE. In comparison to the DPO/BHJ devices obtaining 45.81% of initial PCE after ~ 550 h aging, the BHJ(DPO) devices present superior thermal stability of retaining 61.11% of initial PCE under the identical aging condition, indicating the self-assembly strategy can improve the tolerance to thermal stressing. We speculate

that the interface/boundary of sequential deposition of DPO and BHJ active layer with orthogonal solvent can be the main loss channel to destabilize the DPO/BHJ devices. Whereas the self-assembled BHJ(DPO) devices possess no obvious boundary/interface between DPO and BHJ active layer since they both processed by the same solvent and the self-assembly of DPO on the near ITO side is due to the large surface energy of DPO. These stability results have strictly proven the great potential of self-assembly strategy towards highly stable OSCs.

3. Conclusion

In summary, we demonstrated a green-solvent-processible open-air-printed self-assembly strategy to simultaneously simplify the device architecture, reduce the cost of the printing process, improve the photovoltaic performance and enhance the storage, thermal as well as light illumination stability of organic photovoltaic towards commercialization. The self-assembly strategy prompts the PCEs of BHJ(DPO) devices from 13.0% to 15.5%, which stands the top value for both self-assembled OSCs and blade-coated BHJ OSCs in air. We found that the enhanced photovoltaic performance is originally from i) the finely self-organized DPO-rich region near ITO surface, which coexists harmoniously with PM6 and BTP-ec9 and contributes to the charge extraction and transport; ii) the subtly controlled aggregation rate of both PM6 and BTP-ec9, resulting in suitable phase separation with reduced defects; iii) the self-assembly of DPO induced vertical donor/acceptor phase separation manipulation, leading to relatively more PM6 presented next to the anode side and more BTP-ec9 shown close to the cathode side, which is beneficial for the exciton diffusion and charge collection. In addition, the self-assembly strategy enabled 13.2% efficiency with a device area of 0.98 cm^2 implying its promising potential to scale up production. Our findings demonstrated that this green-solvent-processible open-air-printed self-assembly strategy is beneficial to close the lab-to-fab gap of organic photovoltaic towards commercialized cheap, stable, efficient, scalable, and eco-friendly OSCs.

Conflicts of interest

The authors declare no conflict of interest.

Acknowledgments

H.T. and J. L. contributed equally to this work. S. Lu thanks the research grant from the National Youth Thousand Program Project (R52A199Z11), Chongqing Funds for Distinguished Young Scientists (cstc2020jcyj-jqX0018), Chongqing talent plan (CQYC201903008) and General Program of National Natural Science Foundation of China (62074149). G. Li and K. Liu thanks the support from Research Grants Council of Hong Kong (Project Nos 15221320, C5037-18G, PDFS2021-5S04), Shenzhen Science and Technology Innovation Commission (Project No. JCYJ20170413154602102), the funding for Project of Strategic Importance (Project Code: 1-ZE29), and Postdoctoral Fellowships Scheme (PDFS. Code: YW3Y) provided by the Hong Kong Polytechnic University. K.L. thanks Guangdong Basic Research Foundation (2020A1515110156).

Author contributions

Conceptualization, H. T., S. L., and G. L.; Methodology and critical data curation, H. T., J. L., and K. L.; Writing – original draft, H. T.; Writing – review & editing, H. T., J. L., K. L., Z. R., S. L., and G. L.; In-situ absorption test, K. L., H. T. C., and P. F.; Stability test, Z. R., J. H., and H. X.; DP-XPS and TOF-SIMS test, H. T. C., and Y. Z.; TRPL test, J. K., GIWAX test, J. O., and S. C.; Other data curation, C. Y., S. C., D. H., and H. C.; Supervision, C. Y., Z. K., F. L., S. L., and G. L.

Data availability statement

All data, and materials used in the analysis is available to any researcher for purposes of reproducing or extending the analysis

References

1. Tang, H., *et al.*, *Matter* (2020) **3** (5), 1403
2. Li, G., *et al.*, *Nat. Photonics* (2012) **6** (3), 153
3. Li, G., *et al.*, *Nat. Rev. Mater.* (2017) **2** (8), 17043
4. Zhang, S., *et al.*, *Mater. Today* (2016) **19** (9), 533
5. Yan, C., *et al.*, *Nat. Rev. Mater.* (2018) **3**, 18003
6. Yang, Y., *et al.*, *Nat. Photonics* (2015) **9** (3), 190
7. Cheng, P., *et al.*, *Nat. Photonics* (2018) **12** (3), 131
8. Li, G., *et al.*, *Nat. Mater.* (2005) **4** (11), 864

9. Hou, J., *et al.*, *Nat. Mater.* (2018) **17** (2), 119
10. Baran, D., *et al.*, *Nat. Mater.* (2017) **16** (3), 363
11. You, J., *et al.*, *Nat. Commun.* (2013) **4**, 1446
12. Zhang, J., *et al.*, *Nat. Energy* (2018) **3** (9), 720
13. Tang, H., *et al.*, *Adv. Energy Mater.* (2020) **10**, 2001076
14. Sun, H., *et al.*, *Adv. Mater.* (2021), 2102635
15. Cheng, P., and Yang, Y., *Acc. Chem. Res.* (2020) **53** (6), 1218
16. Huang, J., *et al.*, *Cell Rep. Phys. Sci.* (2021) **2** (1), 100292
17. Huang, J., *et al.*, *Adv. Func. Mater.* (2021) **31** (16), 2010172
18. Liu, Q., *et al.*, *Sci. Bull.* (2020) **65** (4), 272
19. Zhan, L., *et al.*, *Adv Mater.* (2021) **33** (12), 2007231
20. Cui, Y., *et al.*, *Adv Mater.* (2020) **32** (19), 1908205
21. Karuthedath, S., *et al.*, *Nat. Mater.* (2021) **20** (3), 378
22. Lin, Y., *et al.*, *Adv. Mater.* (2015) **27** (7), 1170
23. Wang, J., and Zhan, X., *Acc. Chem. Res.* (2021) **54** (1), 132
24. Yang, W., *et al.*, *Joule* (2021) **5** (5), 1209
25. Sun, R., *et al.*, *Energy Environ. Sci.* (2021) **14** (5), 3174
26. Li, G., *et al.*, *Appl. Phys. Lett.* (2006) **88** (25), 253503
27. Cha, H., *et al.*, *Adv Mater.* (2017) **29** (33), 1701156
28. Wang, Y., *et al.*, *Adv. Energy Mater.* (2019) **9** (19), 1900157
29. Yang, B., *et al.*, *Adv Mater.* (2019) **31** (2), 1804657
30. Zhao, J., *et al.*, *Nat. Energy* (2016) **1** (2), 15027
31. Wadsworth, A., *et al.*, *ACS Energy Lett.* (2017) **2** (7), 1494
32. Qin, D., *et al.*, *J. Mater. Chem. C* (2016) **4** (5), 1051
33. Zhang, H., *et al.*, *J. Mater. Chem. A* (2016) **4** (14), 5032
34. Lin, Y., *et al.*, *Sol. RRL* (2019) **3** (8), 1900179
35. Xiao, Y., *et al.*, *Adv. Energy Mater.* (2021) **11** (21), 2100378
36. Han, X., *et al.*, *Sol. RRL* (2020) **4** (6), 2000108
37. Ye, L., *et al.*, *Chem. Mater.* (2016) **28** (20), 7451
38. Wang, Y., *et al.*, *Adv. Energy Mater.* (2020) **10** (7), 1903609
39. Cheng, P., *et al.*, *Adv. Sci.* (2015) **2** (6), 1500096
40. Zhang, Y., *et al.*, *Nat. Commun.* (2021) **12** (1), 4815
41. Hu, D., *et al.*, *Energy Environ. Sci.* (2020) **13** (7), 2134
42. Lv, J., *et al.*, *Energy Environ. Sci.* (2021) **14** (5), 3044
43. Yan, C., *et al.*, *Adv. Sci.* (2020) **7**, 2000149
44. Tang, H., *et al.*, *Adv. Sci.* (2019) **6**, 1901613
45. Yan, C., *et al.*, *Sol. RRL* (2019) **3**, 201900377
46. Dong, X., *et al.*, *Sol. RRL* (2019) **4** (1), 1900326
47. Ma, R., *et al.*, *Sci. China Chem.* (2020) **63** (3), 325
48. Duan, T., *et al.*, *J. Mater. Chem. A* (2019) **7** (6), 2541
49. Lv, J., *et al.*, *Sol. RRL* (2019) **4** (3), 1900403
50. Hu, D., *et al.*, *Adv. Sci.* (2021) **8** (8), 2004262